

4 **Dynamical behavior of a tensegrity structure**
5 **coupled to a spatial steel grid**
6

7
8
9
10 **ABSTRACT**
11

Aim: In this study it is presented a methodology to determine the structural response of a tensegrity system working under the effects of wind, temperature variations and when coupled to a steel spatial grid applied as pedestrian bridge. This methodology is based in applying nonlinear static and dynamic analyzes and the base motion method.

Place and duration of study: The study was carried out in the Graduate Engineering Department, Universidad Autonoma de Queretaro, Queretaro, Mexico. September 2017 to July 2019.

Methodology: At first instance, it was analyzed the equilibrium configuration of a tensegrity system by only considering self-weight through non-linear static analyzes. In the second stage, it was studied the structural response and internal forces of the proposed tensegrity system under environmental loads as temperature variations and wind forces, which were represented as dynamic effects in a non-linear finite element model. Later, a spatial steel grid was analyzed for such environmental loads but using linear static analyzes. Finally, by applying the principle of superposition to the spatial steel grid, and the base motion method to the tensegrity system, it was represented the coupling of both systems as a single assembly.

Results: The structural response of a tensegrity system when working under different load conditions is obtained. Also, the effects produced by the coupling of both systems are determined.

Conclusion: The study concluded that the tensegrity system shows a stable response for the different load combinations established. There are also denoted the increases in internal forces and displacements for specific loads cases, which may affect locally some components and the overall behavior of the assembly.

12
13 *Keywords: Tensegrity Structures; Static and Dynamic Nonlinear Analysis; Base motion*
14 *Method; Pedestrian bridge.*
15

16 **1. INTRODUCTION**
17

18 Tensegrity structures (TS) are generally attractive to users, they have mechanical
19 characteristics that in comparison to conventional systems, increase their structural
20 efficiency (ratio: load bearing / self-weight) [1]–[3]. TS allow the use of sustainable materials
21 and the implementation of efficient constructive processes, because a large percentage of
22 the structure is work-shop made, this minimizes the building time. TS are pin-jointed free-
23 standing structures, made-up by a continuous red of cables working under tensile forces, in
24 which, isolated bar elements, that works under compression forces are contained [4]. Initially
25 proposed by R. B. Fuller, K. Snelson and G. Emmerich [1], their name is a contraction of the
26 words “tensional integrity”, proposed by R. B. Fuller.

27

28 It is considered that the invention of TS was done in the plastic arts field [1]; however, in the
29 architecture and civil engineering, many structural systems, partially based on the
30 mechanical behavior of TS have been developed, such as the tensile membrane structures
31 from La Plata stadium roof and the Georgia Dome [5]; another example is the Kurilpa bridge,
32 which is claimed as the first hybrid TS implemented in an elevated pedestrian walkway [6].

33

34 In aerospace and robotics fields, TS are applied as folding structures and smart structures,
35 due their capacity to change their shape, by controlling the prestress of cable elements [7].
36 The super ball-bot is one of the ultimate developments of these areas, it was created by
37 NASA as a planetary exploration robot [8].

38

39 From a structural mechanics point of view, progress and knowledge about TS stand out.
40 Current research proposes various techniques and methodologies to perform numerical
41 models [9]. Behavior of TS adapted to work against gravitational static loads has been
42 analyzed by [10], [11]. [5], [12] studied TS under static and dynamic wind forces. In addition,
43 modal parameters have been characterized considering variations in the ambient
44 temperature of some common TS [13].

45

46 However, from the literature review, it is noted that, in current researches, little has been
47 studied about the interaction of environmental effects and the multiple load combinations
48 that would act on a TS exposed to outdoor conditions [14]. The integration of these variables
49 can be carried out through dynamic non-linear methods, since they allow to approximate, to
50 a greater degree, the behavior of TS under the above-mentioned weather load cases.

51

52 It should be noted, the null scope by the building codes, in regards to the analysis and
53 design of tensegrity structures. This fact is one of the main aspects that limit the
54 implementation of TS as civil structures [2], [15]. In the absence of such regulations,
55 researches carried out on these systems, define that stability is the parameter that allows
56 describing the behavior of TS.

57

58 Historically, research about tensegrity systems has focused mainly on the finding form
59 process [16], due to, in assemblies with complex geometries or large amounts of elements,
60 not all the methods converge. Other reason is that current methods do not allow to control
61 the resulting geometric characteristics, or, to keep the principle of mechanical unilaterality for
62 each type of element [17]–[20]. Although it should be noted that the methods developed to
63 date, are convenient and can be adapted or modified to solve a specific system.

64

65 It has been studied the characteristics and conditions to ensure stability of TS, considering
66 self-weight and prestress of cables. Connelly [21] presents a criterion called “Super stability”,
67 through which analyses basic prismatic systems. Subsequently, [22] defines two concepts of
68 stiffness for TS, that are named “Prestress stability” and “Second order stiffness”, by which,
69 stability is provided to the TS. Similarly, Deng and Kwan [23] propose a general classification
70 of the necessary conditions to determine the stability of an ET, by analyzing the tangential
71 stiffness matrix and considering the variations of the potential energy of the second order.
72 Complementing these works, Zhang and Ohsaki [24] formally establish the conditions
73 required for an TS to be stable, which are based in the fact that the tangent stiffness matrix
74 must be defined and positive. Their conclusions states that the minimum necessary
75 conditions are: the force density matrix must be positive and defined, in addition to having a
76 minimum range deficiency equal to $d + 1$; and, the range of the geometric stiffness matrix
77 should be $d(d + 1) / 2$; where d is the vector of non-trivial displacements.

78

79 Subsequently, TS structural response was characterized under the effects of external loads
80 as compression, tension and torsion. Lazopoulos [25] employs the bifurcation method, to
81 study the conditions that generate global and local instabilities in a 3-plex system. Amendola
82 [26] studied the behavior of the 3-plex system, considering compressive loads for two
83 boundary conditions cases at the base nodes: with total restriction of movement, and, with
84 freedom of movement in the horizontal plane. From case 1, it is shown that the structure
85 tends to stiffen when the load is applied, and for the second case, 3-plex systems presents a
86 softening behavior. 3-plex system was also studied by Zhang *et al.* [27], who identified that,
87 when acting torsional loads, a new type of instabilities appears which were named 'Snapping
88 Instabilities'. It was observed that this behavior was present in the transition of equilibrium
89 states, once the system was loaded. Snapping instability occurs when torsional load is
90 higher than the allowable, which generates permanent deformations, even when the
91 elements work within the elastic limit. Atig *et al.* [28] discuss the possible existence of
92 dynamic instabilities in the 3-plex system and in the Geiger dome. This effect was observed
93 when systems were excited with white noise, and is associated to slackening of cables
94 during loading cycles.

95
96 The previously presented works identify that some systems may present instabilities caused
97 by external loads. In addition, there is a lack of knowledge about the response of tensegrity
98 systems applied in cases other than light-weight roofs, where the interaction of wind effects
99 with temperature variations is included. Therefore, this work presents the study and
100 development of a stable tensegrity system, under dynamic environmental loads. This
101 tensegrity structure will be coupled to the superstructure of a pedestrian bridge, applying the
102 "ground motion" method, in order to represent the behavior of whole assembly under the
103 described external loads.

104 **2. MATERIAL AND METHODS**

105 **2.1 Superstructure description for the proposed Pedestrian Bridge.**

106
107
108
109 Superstructure of the pedestrian bridge is composed by two different systems: the main
110 structure of the bridge, which consist of a single-lattice spatial layer grid (also known as
111 spatial double layer grid, SDLG), and by five identical tensegrity modules, which are the
112 result of this research, and will be coupled to the main structure.

113
114 SPLG is integrated by the parts indicated in Fig. 1. It has a total length of 28.0 m, width of
115 2.80 m, and 1.50 m for height; covering a clear span of 22.0 m. It is proposed a floor system
116 by precast W-deck panels whose weight is 200 kg/m^2 , and will be mounted on a steel
117 support system, that will allow their installation. Per the Mexican standards for bridges [29]
118 live load will be considered as 400 kg/m^2 . Table 1 shows the mechanical properties of the
119 structural elements used for this system.

120

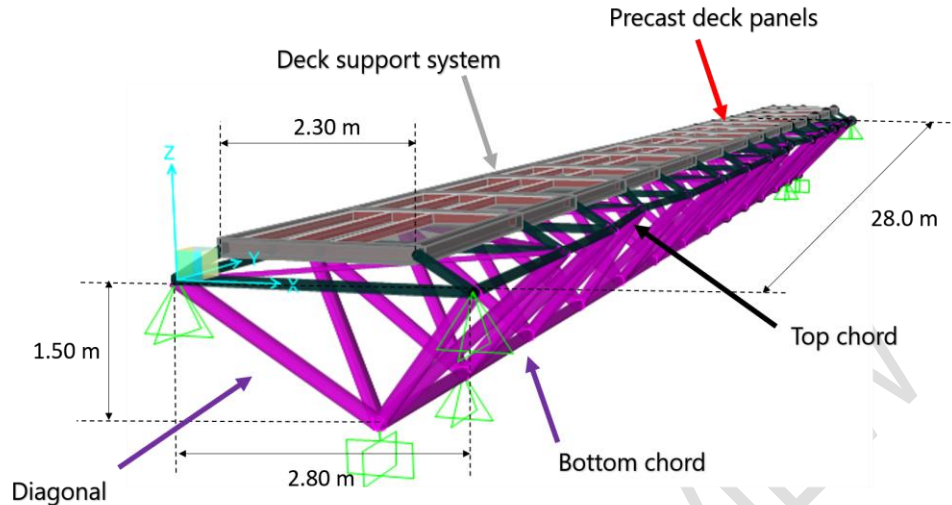


Fig. 1. 3D view of the SDLG.

121
122
123
124
125

Table 1. Mechanical properties of the SDLG components

Cross-section type	Round HSS	Rectangular HSS	Round tubes
ASTM Nom.	A500 Gr. 42	A500 Gr. 46	A53 Gr. B
Yield Stress (Fy)	2952 kg/cm ²	3234 kg/cm ²	2460 kg/cm ²
Ultimate Stress (Fu)	4077 kg/cm ²	4077 kg/cm ²	4218 kg/cm ²

126
127
128
129
130

Fig. 2 shows a view in the X-Y plane, at a height of 0.0 m. This geometric configuration allows the coupling of the five tensegrity modules, whose location corresponds to the dotted areas of green and blue.

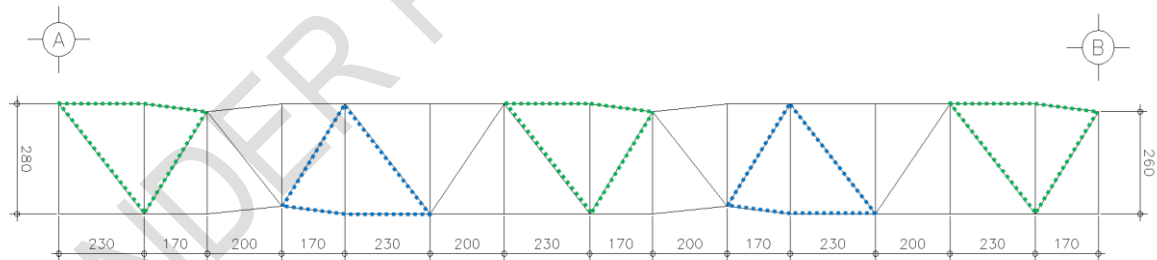


Fig. 2. View in the X-Y plane of the SDLG, Z = 0.0 m.

131
132
133
134
135
136
137
138
139
140
141
142
143

The tensegrity module developed in this work is called "X-T". Topology and connectivity of the X-T module are described by Fig. 3. The X-T system consists of 27 elements, of which 5 elements are bar type and 22 elements are cable type, which converge to 10 nodes. This assembly was developed with the aim of establishing a tensegrity system, whose geometrical and architectural features allow pedestrian traffic, when implemented on a pedestrian bridge. The interior clearance of the X-T module (Fig. 4a and 4b) is 2.70 m wide and 2.80 m high. The total width is 4.90 m, its length is 3.8 m and the total height is 5.45 m.

The spatial configuration of the X-T module was obtained by applying a form finding method based on the double decomposition of singular values, initially proposed by Yuan [18]. The

144 nodal coordinates of the system are shown in table 2, and, in table 3, the mechanical
 145 characteristics of the materials that make up this system are shown.

146
 147
 148

Table 2. Nodal coordinates

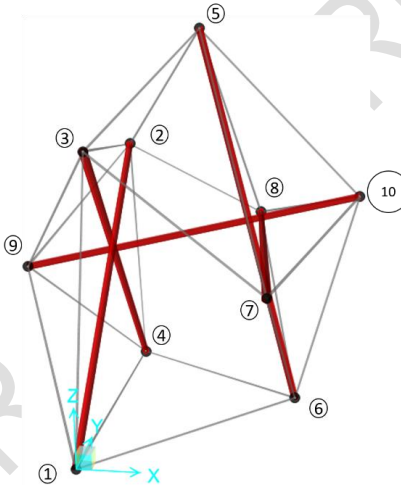
Node	X	Y	Z	Node	X	Y	Z
1	0.000	0.000	0.000	6	2.800	2.300	0.000
2	0.000	3.800	3.800	7	2.261	-0.829	2.500
3	0.200	0.000	3.900	8	2.261	4.829	2.500
4	0.200	4.000	0.000	9	-1.300	2.200	2.000
5	1.336	2.000	5.464	10	3.613	2.200	3.146

149
 150
 151

Table 3. Mechanical properties of the tensegrity components

Element type	Bar	Cable
ASTM Nom.	Aluminum 6063 T6	A586 Class A.
Modulus of elasticity	710100.3 kg/cm ²	1687367.1 kg/cm ²
Yield Stress (Fy)	1757.67 kg/cm ²	10546 kg/cm ²
Ultimate Stress (Fu)	2109.21 kg/cm ²	15467.5 kg/cm ²

152



153
 154
 155

Fig. 3. Perspective view and node numbering of the X-T module.

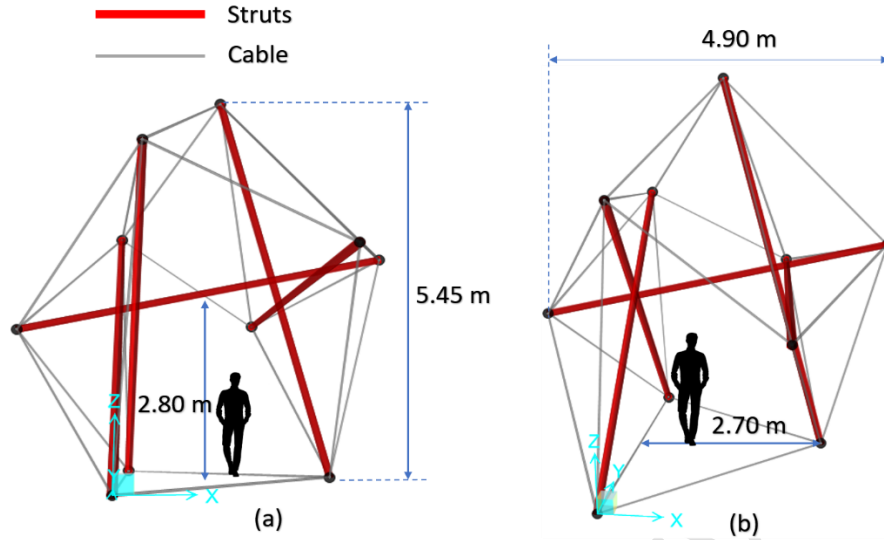


Fig. 4. External and internal dimensions of the X-T module.

156
157
158
159
160
161
162
163
164
165
166
167
168

2.2 Mathematical framework

Several authors have investigated and contributed to determine the mathematical models that represent the mechanical behavior of tensegrity structures [30], [31]. Murakami [10]-[11] shows in detail the basic equations for static and dynamic analyzes, both in Eulerian and Lagrangian formulations. Mechanical principles that must be met, refer in particular to the equilibrium the system, compatibility between displacements and deformations, and the relationships between internal and external forces. These conditions, which are actually general for any mechanical system, can be stated in tensorial expressions as follows:

a) Equilibrium equation

$$\text{Div} \underline{\underline{S}} + \underline{\underline{b}} = \rho \dot{\underline{\underline{v}}} \quad (1)$$

169 b) Strain-Displacement Relation

$$\underline{\underline{E}} = \frac{1}{2} (\nabla \underline{\underline{u}} + \nabla \underline{\underline{u}}^T) \quad (2)$$

170 c) Strain-Stress Relation (Compatibility equation)

$$\underline{\underline{S}} = \underline{\underline{C}} [\underline{\underline{E}}] = 2\mu \underline{\underline{E}} + \lambda (\text{tr} \underline{\underline{E}}) \underline{\underline{I}} \quad (3)$$

171 Where:

172 $\underline{\underline{E}}$: Deformation tensor. Second-order tensor formed as:

$$\underline{\underline{E}} = \sum_{i,j} E_{ij} \mathbf{e}_i \otimes \mathbf{e}_j \quad (4)$$

173 $\underline{\underline{C}}$: Elasticity tensor. Fourth-order tensor.

174 $\underline{\underline{I}}$: Identity tensor.

175 $\underline{\underline{S}}$: Piola-Kirchhoff stress tensor. Second-order tensor.

176 $\underline{V}u$: Deformation gradient
 177 \underline{b} : Body forces field
 178 ρ : Density field
 179 $\underline{\dot{v}}$: Acceleration field
 180 μ, λ : Lamé parameters

181

182 2.3 Finite Element Method

183

184 Tensegrity structures have a non-linear behavior when working under external loads,
 185 because, both the stiffness of the system and the loads, are in function of displacements and
 186 / or deformations, which are generally of great magnitude in such type of systems. On the
 187 other hand, prestress of cable elements generates a non-linear geometric effect on the
 188 system [32]. In this work, only the nonlinear geometric effects in the elastic range of the
 189 cable elements will be considered.

190

191 Finite element method (MEF) is a numerical procedure used to find an approximate solution
 192 of partial differential equations that allow modeling a physical system. The discrete model
 193 associated to the mechanical behavior of a system is as follows:

194

$$\left\{ \int_V [B]^T [D] [B] dV + \int_V [G]^T [M] [G] dV \right\} \{U\} = \int_V [N]^T \begin{Bmatrix} b_x \\ b_y \\ b_z \end{Bmatrix} dV + \int_V \{\varepsilon_0\}^T [D] \{\varepsilon_0\} dV + \begin{Bmatrix} F_x \\ F_y \\ F_z \end{Bmatrix} \quad (5)$$

195

196 where [B] is the derivations shape functions matrix, [E] is the elastic constants matrix, [G]
 197 the partial derivations shape functions matrix, [M] is the membrane forces matrix, {U} is the
 198 nodal displacement vector, [N] is the shape functions matrix, {bx by bz}^T is the body forces
 199 vector, {ε₀} is the vector of residual stresses associated with temperature variation and {F_x
 200 F_y F_z}^T is the vector of nodal external forces.

201

202 The mathematical model of equation (5) can be represented in simplified form as:

$$[K_t] \{U\} = \{[K] + [K_G]\} \{U\} = \begin{Bmatrix} W_x \\ W_y \\ W_z \end{Bmatrix} + \begin{Bmatrix} \varepsilon_x \\ \varepsilon_y \\ \varepsilon_z \end{Bmatrix} + \begin{Bmatrix} F_x \\ F_y \\ F_z \end{Bmatrix} \quad (6)$$

203 where [K_t] is the tangent stiffness matrix, [K] is the elastic stiffness matrix, [K_G] is the
 204 geometrical stiffness matrix, {W_x W_y W_z}^T is the force vector associated to the self-weight of
 205 each element, and {ε_x ε_y ε_z}^T is the vector of residual forces related with temperature
 206 variations [33].

207

208 2.4 Static nonlinear analysis

209

210 The solution of the TS will be carried out applying an iterative-incremental method for
 211 nonlinear structural analysis, called Newton-Raphson [34]. In terms of FEM, the equations
 212 system is expressed as:

$$[K_t] \Delta \{U\}^j = \begin{Bmatrix} W_x \\ W_y \\ W_z \end{Bmatrix} + \begin{Bmatrix} \varepsilon_x \\ \varepsilon_y \\ \varepsilon_z \end{Bmatrix} + \begin{Bmatrix} F_x \\ F_y \\ F_z \end{Bmatrix} \quad (7)$$

213 where Δ represents the variations at the "j" iteration in the displacement vector $\{U\}$.

214

215 For bar elements, where only act axial effects, the stiffness matrices are structured as
216 follows:

$$[K] = \left(\frac{EA}{L}\right) \begin{bmatrix} 1 & 0 & 0 & -1 & 0 & 1 \\ 0 & 0 & 0 & 0 & 0 & 0 \\ 0 & 0 & 0 & 0 & 0 & 0 \\ -1 & 0 & 0 & 1 & 0 & -1 \\ 0 & 0 & 0 & 0 & 0 & 0 \\ 0 & 0 & 0 & 0 & 0 & 0 \end{bmatrix} \quad (8)$$

$$[K_G] = \left(\frac{T}{L}\right) \begin{bmatrix} 1 & 0 & 0 & -1 & 0 & 0 \\ 0 & 1 & 0 & 0 & -1 & 0 \\ 0 & 0 & 1 & 0 & 0 & -1 \\ -1 & 0 & 0 & 1 & 0 & 0 \\ 0 & -1 & 0 & 0 & 1 & 0 \\ 0 & 0 & -1 & 0 & 0 & 1 \end{bmatrix} \quad (9)$$

217 where E is the modulus of elasticity of the material, A is the cross-sectional area of each
218 element, L is the length of the element and T is the internal membrane force, a value that is
219 naturally associated with prestress of the cable elements.

220

221 2.5 Dynamic nonlinear analysis

222

223 Nonlinear dynamic models will be used to represent the effects of wind and the coupling of
224 tensegrity systems with the SDLG, such as forces and displacements as a function of time.
225 The characteristic equation for the dynamic equilibrium problems is:

226

$$[M]\{\dot{U}\}_{n+1}^j + [C]\{U\}_{n+1}^j + [K_t]\{U\}_{n+1}^j = P(t) \quad (10)$$

227 with P(t) defined as:

$$P(t) = \begin{Bmatrix} W_x \\ W_y \\ W_z \end{Bmatrix}_{n+1} + \begin{Bmatrix} \varepsilon_x \\ \varepsilon_y \\ \varepsilon_z \end{Bmatrix}_{n+1} + \begin{Bmatrix} F_x \\ F_y \\ F_z \end{Bmatrix}_{n+1}^j \quad (11)$$

228 where [M] is the mass matrix, $\{\ddot{U}\}$ is the vector of acceleration, [C] is the damping matrix, $\{\dot{U}\}$
229 is the velocity vector. "n" represents the current incremental step and "j" represents the next
230 incremental step [35].

231

232 2.5.1 Pulse-type Excitation Function

233

234 Particularly, the force of the wind acting on the structure will be represented with a pulse-
235 type excitation function, with the aim of idealizing a gust of wind that will act for an interval t
236 $= 4$ s, and then cease. Figure 5 shows the diagram of the proposed function to model the
237 wind gust [35].
238

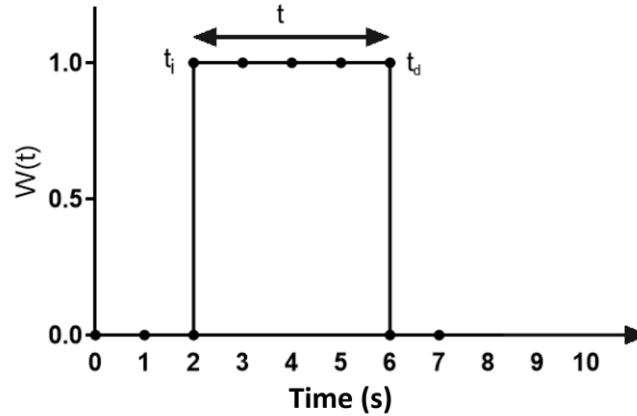


Fig. 5. Pulse-type Excitation Function.

239

240

241

242 Considering the initial conditions $u(0) = 0$, $\dot{u}(0) = 0$, with a value damping of 2.4%, the
 243 solution for this type of excitation is:

244

$$u(t) = \frac{P_0}{k} \left[1 - e^{-\zeta\omega_n t} \left(\cos(\omega_d t) + \frac{\zeta\omega_n}{\omega_d} \sin(\omega_d t) \right) \right] \quad (12)$$

245

246

247

2.5.2 NEWMARK-BETA METHOD OF DIRECT INTEGRATION

248 Direct integration methods are used to solve initial value problems by a step-by-step
 249 integration with respect to time [35], [36]. It is assumed that both displacements $\{U\}$ and
 250 velocities $\{\dot{U}\}$ are known at a given time $t = 0$ s. The solution obtained with this method is
 251 given through an incremental approximation process.

252

253 Newmark-Beta method states that, considering the mean value theorem, the first derivative
 254 of displacement, can be solved as:

255

$$\dot{u}_{n+1} = \dot{u}_n + \Delta t \ddot{u}_\gamma \quad (13)$$

256 where:

$$\ddot{u}_\gamma = (1 - \gamma)\ddot{u}_n + \gamma\ddot{u}_{n+1} \quad (14)$$

257 with $0 < \gamma < 1$. Thus:

$$\dot{u}_{n+1} = \dot{u}_n + \Delta t((1 - \gamma)\ddot{u}_n + \gamma\ddot{u}_{n+1}) \quad (15)$$

258 Since acceleration also varies over the time, the average value theorem will be used again
 259 to calculate the second derivative of the displacement.

260

$$u_{n+1} = u_n + \Delta t \dot{u}_n + \frac{1}{2} \Delta t^2 \ddot{u}_\beta \quad (16)$$

261

with $0 < \beta < 1$. In this way:

262

$$\ddot{u}_\beta = (1 - 2\beta)\ddot{u}_n + 2\beta\ddot{u}_{n+1} \quad (17)$$

263 For this method a value of 0.5 for α and 0.25 for β are suggested, which gives stability to
 264 the method. Which is expressed as:
 265

$$\dot{u}_{n+1} = \dot{u}_n + \frac{\Delta t}{2}(\ddot{u}_n + \ddot{u}_{n+1}) \quad (18)$$

266

$$u_{n+1} = u_n + \Delta t\dot{u}_n + \frac{1 - 2\beta}{2}\Delta t^2\ddot{u}_n + \beta\Delta t^2\ddot{u}_{n+1} \quad (19)$$

267

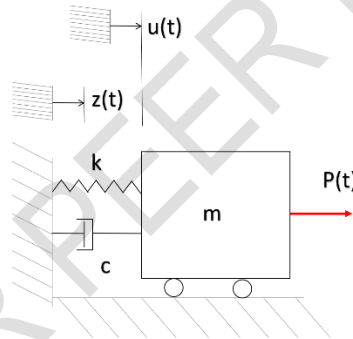
268 2.5.3 BASE MOTION METHOD

269

270 When the supports of a structural system produce or transmit actions to the structure, as
 271 manner of movement (Fig. 6), it is convenient to propose equation (10), in function on the
 272 relative displacements as follows [35], [36]:
 273

$$[M]\{\dot{U}\}_{n+1}^j + [C]\{\dot{U} - \dot{Z}\}_{n+1}^j + [K_t]\{U - Z\}_{n+1}^j = P(t) \quad (20)$$

274



275 **Fig. 6. Representative system of the base motion method.**

276

277

278

279

Expressing equation (20) as a relative displacements $W = U - Z$, $\dot{W} = \dot{U} - \dot{Z}$ y $\ddot{W} = \ddot{U} - \ddot{Z}$,
 results:

$$[M]\{\dot{W}\}_{n+1}^j + [C]\{\dot{W}\}_{n+1}^j + [K_t]\{W\}_{n+1}^j = P(t) - [M]\{\dot{Z}\}_{n+1}^j \quad (21)$$

280

281

282

283

284

285 2.6 Methodology

286

287

288

289

290

291

In the first instance, non-linear static analyzes of the tensegrity system were carried out, in the software SAP2000 [37], to determine the spatial configuration and internal axial forces associated with the equilibrium of the system under gravitational effects. The boundary conditions of the support nodes are shown in table 4.

292 **Table 4. Boundary Conditions of base nodes.**

293

Node	Ux	Uy	Uz
1	Fixed	Fixed	Fixed
4	Fixed	Free	Fixed
6	Fixed	Free	Fixed

294

295 It is considered that the pedestrian bridge will be located in Queretaro, Mexico. For this site it
 296 is estimated a wind speed for design of 101.8 km/hr and a wind pressure of 77.83 kg/m²
 297 [38]. The maximum average temperature in summer is 31 ° C and in winter it is 23.3 ° C;
 298 while the minimum average temperature in summer is 15°C and in winter it is 7°C [39].
 299 Therefore, two cases of thermal variation will be analyzed, an increase of 16°C and a
 300 decrease of 16°C.

301

302 Both structures were analyzed with independent finite element models, applying the Mexican
 303 standards for design of pedestrian bridges [38]. Load combinations for the SDLG analysis
 304 are shown in table 5. For service and work load combinations, the coefficient ζ is equal to 1,
 305 while for design combinations it will have a value of 1.25 for CT-2 and CT-3 cases, and,
 306 equal to 1.40 for CT-5 y CT-6 cases. The value of γ is equal to 1 service load combinations.
 307 On the other hand, for design combinations, this coefficient will take a value of 1.30 for FC-2
 308 y FC-3, and, 1.25 for FC-5 y FC-6 cases.

309

310 **Table 5. Load combinations for SDLG**

311

Service and work load combinations		Design load combinations	
CT-2	$\zeta^* (W)$	FC-2	$\gamma^* (\beta_{CM}DL + W)$
CT-3	$\zeta^* (DL + Sw + LL + 0.3W + WLL)$	FC-3	$\gamma^* (\beta_{CM}DL + Sw + 1.2LL + 0.3W + WLL)$
CT-5	$\zeta^* (DL + Sw + W + T)$	FC-5	$\gamma^* (\beta_{CM}DL + Sw + W + T)$
CT-6	$\zeta^* (DL + Sw + LL + 0.3W + WLL + T)$	FC-6	$\gamma^* (\beta_{CM}DL + 1.2LL + 0.3E + WLL + T)$

312

313 Nomenclature of the loads shown in table 5 is: DL = Dead load, LL = Live load, W = Wind
 314 force on the structure, WLL = Wind over the live load, and, T = Temperature. β_{CM} is equal to
 315 1.0 for bending and pure tension elements. While, for elements working under bending and
 316 compression simultaneously, there are the following cases: $\beta_{CM} = 1.0$, for the condition of
 317 maximum axial load and minimum bending moment; $\beta_{CM} = 0.75$, for the condition of
 318 minimum axial load and maximum bending moment.

319

320 Load combinations for the TS are shown in table 6.

321

322 **Table 6. Load combinations for the tensegrity structure**

323

Load combination	
Comb. 1	$\zeta^* (Sw + Press + W)$
Comb. 2.a	$\zeta^* (Sw + Press + D16^\circ C)$
Comb. 2.b	$\zeta^* (Sw + Press + D16^\circ C + W)$
Comb. 3.a	$\zeta^* (Sw + Press - D16^\circ C)$
Comb. 3.b	$\zeta^* (Sw + Press - D16^\circ C + W)$

324

325 Where "Sw" refers to self-weight, "Press" to the prestress in cables, and W to the wind load
 326 acting over the structure. These load cases are described below:

327

328 In the load comb. 1, the structure was subjected to dynamic wind forces and temperature
329 was considered constant ($\Delta T=0^{\circ}\text{C}$). At load combinations of group 2, it was first induced a
330 16°C ($\Delta T=+16^{\circ}\text{C}$) increase in temperature (comb. 2.a) and subsequently, the wind forces
331 were applied as a dynamic function (comb. 2.b). Similarly, for the load combinations of group
332 3, it was considered a 16°C ($\Delta T=-16^{\circ}\text{C}$) decrease in temperature (comb. 3.a), prior to the
333 application of wind forces on the system (comb. 3.b).

334

335 Analysis of SDLG was performed based on linear static models, where loads were idealized
336 as constants. On the other hand, for TS, analyses were carried out by nonlinear static and
337 dynamic models (see sections 2.4 and 2.5).

338

339 Once the internal forces, reactions and maximum nodal displacements of each system were
340 determined, the actions between both systems were transferred. It was identified that the TS
341 transfers loads to the SDLG, through its support nodes, effect that was represented by the
342 superposition principle. In contrast, at those nodes of the SDLG, which join with the base
343 nodes of TS, there were observed differential displacements, which were modeled as a
344 dynamic problem of base motion.

345

346 The load cases, load combinations and the methodology presented throughout current
347 section, were used to compute the mathematical models of both structural systems by
348 means of SAP2000 software [37].

349

350 3. RESULTS AND DISCUSSION

351

352 The spatial configuration of the X-T module and the initial prestress values were obtained
353 through the form finding process proposed by [18], which are the initial parameters to
354 perform the nonlinear static analysis. Using the software SAP2000 [37], based on the finite
355 element method, the results shown below were obtained.

356

357 3.1 Static nonlinear analysis under self-weight (Sw).

358

359 Static nonlinear analysis when only considering self-weight load case (Sw) of the X-T,
360 module gives as result the spatial configuration shown in table 7 (Fig. 7) and the axial forces
361 from table 8 and 9, in the column "Sw".

362

363 By comparing the nodal coordinates of table 7 against the resulting coordinates of the
364 search process so (see Table 2), it is observed that the higher order difference is 0.39 cm in
365 the X axis at the node 7.

366

367 The maximum variation of axial force for bar elements occurs in the element 1, with an
368 increase of 47 kg, equivalent to 4.7%. In cable elements, the maximum increase occurs in
369 element 21, with a value of 30 kg, corresponding to an increase of 22.6%.

370

371

372 **Table 7. Resulting nodal coordinates of the X-T module from a static nonlinear**
373 **analysis considering self-weight.**

374

Node	X	Y	Z	Node	X	Y	Z
1	0.000	0.000	0.000	6	2.800	2.301	0.000
2	-0.004	3.801	3.799	7	2.257	-0.828	2.499
3	0.196	0.000	3.899	8	2.284	4.877	2.525
4	0.200	4.001	0.000	9	-1.302	2.200	1.998
5	1.332	2.000	5.463	10	3.610	2.200	3.146

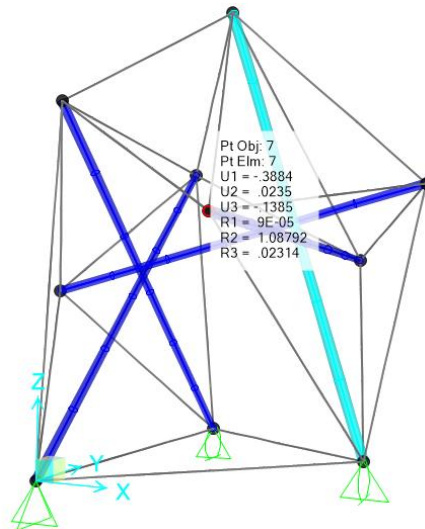


Fig. 7. Spatial configuration of X-T module under self-weight effects.

376
377
378
379
380
381

3.2 Structural response and internal forces variations of the “X-T” module, due dynamic meteorological actions.

382
383
384
385

To study the behavior of the X-T module under the load combinations defined in Table 6, dynamic non-linear models were performed, with the aim of determining if the structural system is stable under these working conditions.

386
387
388
389
390
391
392

In the first instance the effects produced in some representative elements of the system are described below. For this, the axial force time-history graphs of bar 3 (Fig. 8 and 11), cable 18 (Fig. 9 and 12) and cable 19 (Fig. 10 and 13) are presented, in addition to the columns of load combination groups 1, 2 and 3, at tables 8 and 9. The initial value of the axial force of the time history records corresponds to the axial force resulting from static nonlinear analysis from section 3.1. From $t = 0$ s to $t = 2$ s, the system is in equilibrium; from $t = 2$ s to $t = 6$ s, is the excitation period; and $t = 6$ s onwards is the free vibration period (see Fig. 5).

393
394
395
396
397
398
399

The results from combination 1, correspond to the effects of self-weight, prestressing and wind action. It is observed that, during the excitation period, the axial force on bar 3 (Fig. 8) increases up to 2450 kg, when the wind acts in the X direction. In the free vibration period, residual oscillations of axial force are observed, in a range of ± 100 kg, which are the product of the internal equilibrium processes of the tensegrity system, and show a decreasing trend over time.

400
401
402
403
404
405
406
407
408

Similar behavior is observed for cables 18 and 19, since, during the excitation period, the axial force increases to 1194 kg (Fig. 9) and 1109 kg (Fig. 10), respectively. However, it is observed that, in the cable 19, when the wind acts the negative X direction (X_n), the axial force is reduced to 0 kg. Subsequently, in the period of free vibration, it is observed that when the external effects culminate, the system has the ability for each element to recover the axial force in equilibrium. For both elements, observed oscillations shown a decreasing tendency of axial force, from ± 50 kg and ± 70 kg, to 0 kg, respectively.

409
410
411

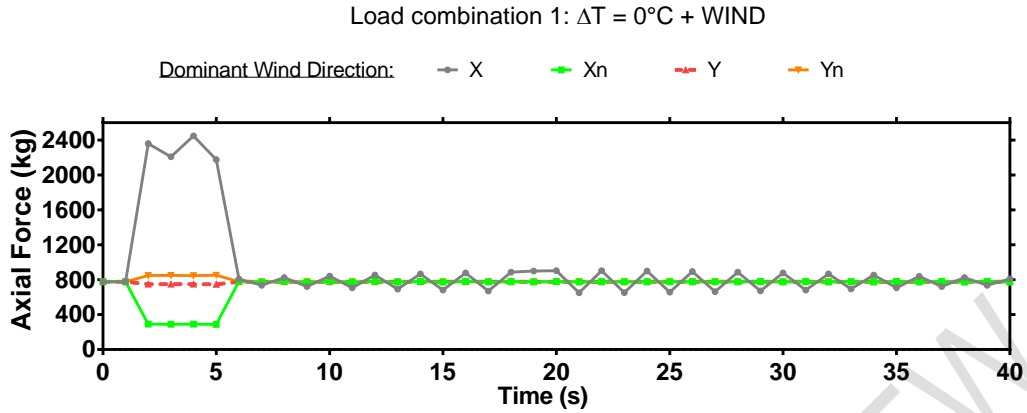


Fig. 8. Time-history record of axial force for bar 3, load combination 1.

412
413
414

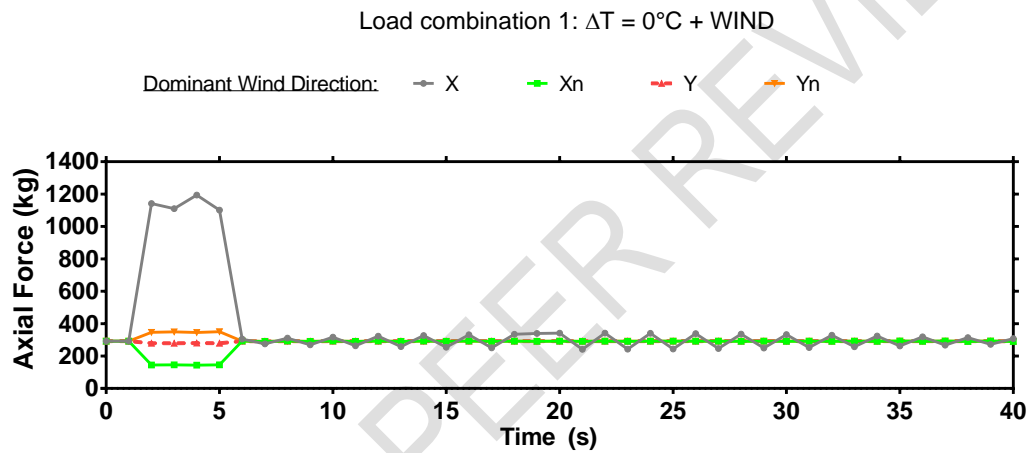


Fig. 9. Time-history record of axial force for cable 18, load combination 1.

415
416
417
418
419

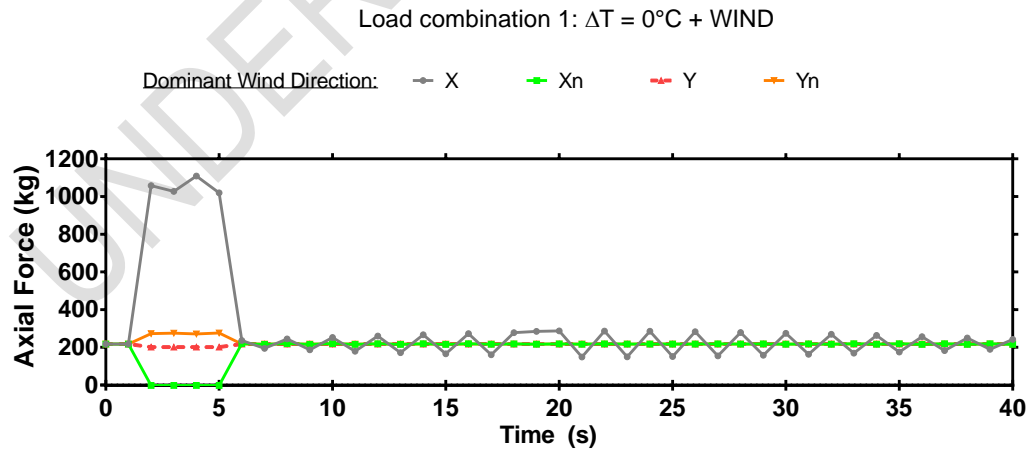


Fig. 10. Time-history record of axial force for cable 19, load combination 1.

In the load combinations 2.a and 3.a, the effects of self-weight, prestress and thermal variation are related. Overall, with the exception of cables 26 and 27, it was recorded that,

420 due to an increase in temperature, the axial force of the elements increases, because of
421 volumetric expansion. In contrast, when temperature decreases, the axial force is reduced,
422 given the contraction that is caused in the structural elements. For cables 26 and 27, an
423 inverse behavior is observed to that described previously, since, under an increase in
424 temperature, the tension of cables 26 and 27 decreases, whereas, when a temperature
425 decrease occurs, their axial force increases.

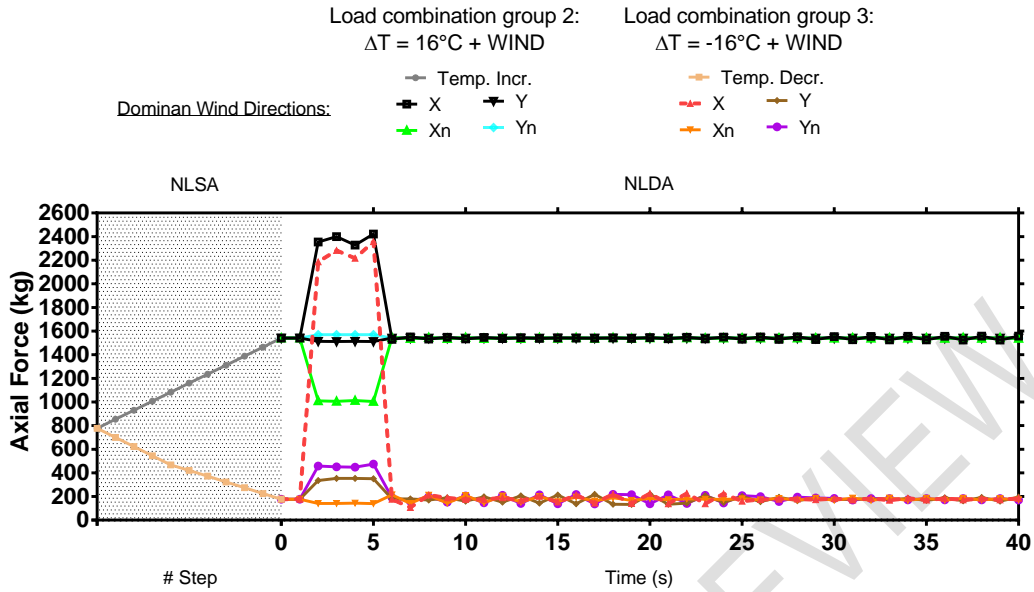
426
427 The results generated by combining the thermal variations together with the wind action, the
428 effects of the own weight and the prestressing (combos 2.b and 3.b) are presented below.

429
430 For bar 3 (Fig. 11) corresponding to the load combination 2.b, it is observed that the axial
431 force increases to 2422 kg, whereas, for the load combo 3.b, compression on bar 3 reaches
432 a value of 2357 kg. In the free vibration period, it is observed that the oscillations of axial
433 force are reduced to a range of 5 kg, for combination 2.b, and to 15 kg for the case 3.b,
434 which decreases with time.

435
436 For cables 18 and 19, in the load combination 2.b, there are increases of the tensile forces
437 up to 1163 kg and 1060 kg. While, in the load combo 3.b, axial forces of 1205 kg (Fig. 12)
438 and 1119 kg (Fig. 13) are reached, respectively. Within the load combo 2.b, the oscillations
439 of axial forces are reduced to a range of 5 kg for both elements; while in the case 3.b, the
440 range of oscillations is reduced to 20 kg. In both load combinations, the tendency of
441 oscillations is decreasing.

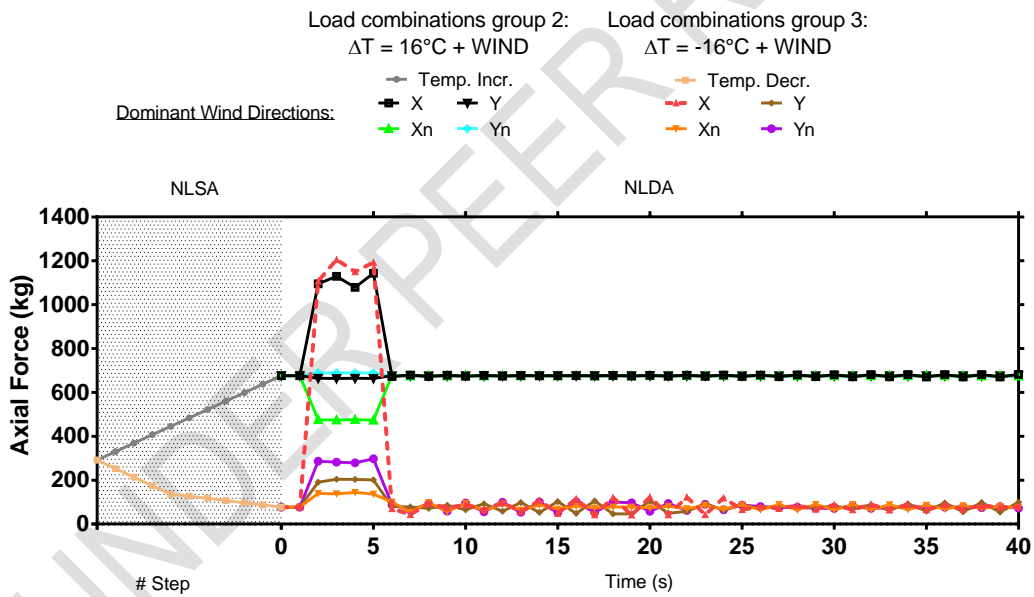
442
443 The behavior described previously, can be generalized for most of the components of the
444 assembly, and the axial forces acting on each element are shown in tables 8 and 9, in the
445 columns for load combinations groups 2 and 3. From these results, it is highlighted that the
446 maximum axial force to which each element is subjected, is caused by a specific wind
447 direction, which will be named dominant wind direction (DWD). In addition, a temperature
448 increase (combo 2.a) can produce a rise in axial forces up to 737 kg in the bar-type
449 elements, and 398 kg in the cable elements; and the decrease in temperature (combo 3.a)
450 produces variations of -627 kg in the bars and -356 kg in the cables. The inclusion of thermal
451 variations together with the action of the wind produces variations of up to 851 kg in the
452 cables and 1618 kg in the bars for the load combination 2.b. In the combination 3.b, the
453 maximum variation is 1553 kg in the bar-type elements and 913 kg in the cables.

454



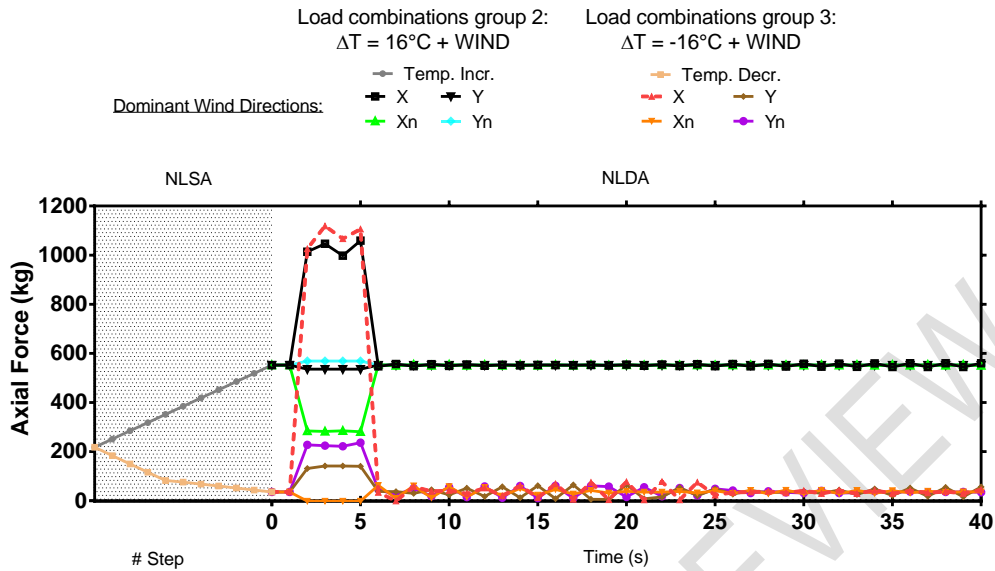
455
456
457

Fig. 11. Time-history record of axial force for bar 3, load combination groups 2 and 3.



458
459
460
461

Fig. 12. Time-history record of axial force for cable 18, load combination groups 2 and 3.



462
463
464
465
466
467
468

Fig. 13. Time-history record of axial force for cable 19, load combination groups 2 and 3.

Table 8. Maximum axial compression forces of bar elements for self-weight analysis and for the load combination groups 1, 2 and 3.

Bar	Sw.			Load comb. group 2 (ΔT=+16°C)			Load comb. group 3 (ΔT=-16°C)		
	Axial Force (kg)	Axial Force (kg)	DWD	Axial Force (kg)	Axial Force (kg)	DWD	Axial Force (kg)	Axial Force (kg)	DWD
1	1047	1369	Yn	1663	2002	Yn	423	1263	X
2	834	1044	Y	1337	1560	Y	317	969	X
3	804	2450	X	1541	2422	X	177	2357	X
4	639	1022	Xn	1164	1543	Xn	152	875	Xn
5	418	1091	X	916	1110	Xn	123	1101	X

469
470
471
472

Table 9. Maximum axial tension forces of cable elements for self-weight analysis and for the load combination groups 1, 2 and 3.

Cable	Sw.			Load comb. group 2 (ΔT=+16°C)			Load comb. group 3 (ΔT=-16°C)		
	Axial Force (kg)	Axial Force (kg)	DWD	Axial Force (kg)	Axial Force (kg)	WDD	Axial Force (kg)	Axial Force (kg)	DWD
6	472	662	Y	782	963	Yn	116	354	Y

7	501	675	X	747	937	Y	191	640	X
8	458	624	Xn	588	774	Xn	211	359	Xn
9	505	677	X	771	921	X	183	652	X
10	263	594	X	445	620	X	54	544	X
11	377	653	X	697	804	Xn	67	581	X
12	371	629	X	677	779	Xn	64	563	X
13	280	618	X	470	639	X	52	544	X
14	298	566	X	566	680	Yn	96	600	X
15	414	868	X	812	950	Yn	141	896	X
16	121	500	X	346	489	Y	25	502	X
17	71	365	X	346	489	Y	25	502	X
18	292	1194	X	676	1143	X	77	1205	X
19	221	1109	X	552	1060	X	35	1119	X
20	164	557	Xn	309	689	Xn	61	547	Xn
21	182	585	Xn	347	734	Xn	67	574	Xn
22	75	282	Xn	152	348	Xn	29	283	Xn
23	94	327	Xn	192	411	Xn	36	326	Xn
24	149	631	X	336	614	X	35	640	X
25	115	508	X	268	485	X	22	505	X
26	96	253	Y	6	181	Y	175	347	Y
27	107	201	Yn	2	200	Yn	199	261	Xn

473
474
475
476
477
478
479
480

On the other hand, the registered nodal displacements from the dynamic analyzes are shown in Table 10. It is observed that the greatest displacements occur in the load combination 3.b, with a magnitude of 6.74 cm, at the free node 7, and of -0.34 cm for the base node 4.

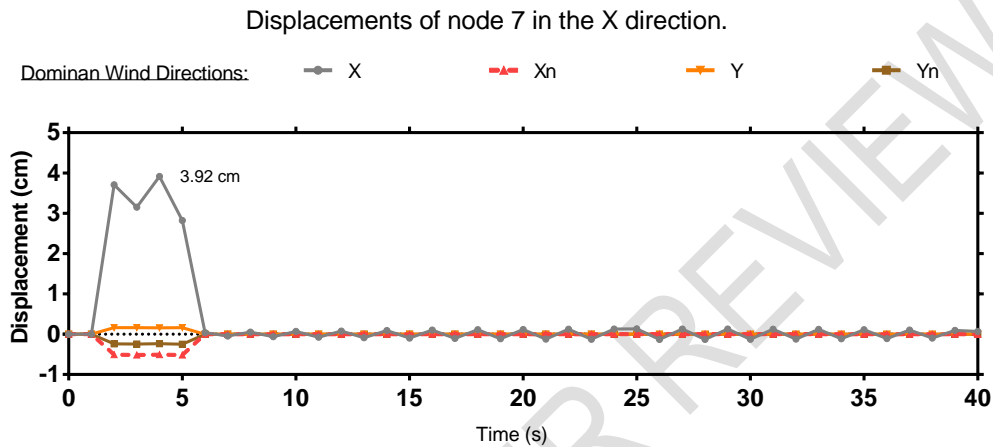
Table 10. Maximum nodal displacements for the load combination 1, 2.b and 3.b.

Node	Case 1 ($\Delta T=0^{\circ}\text{C}$) Wind effects				Case 2.b ($\Delta T=+16^{\circ}\text{C}$) Thermal + Wind effects				Case 3.b ($\Delta T=-16^{\circ}\text{C}$) Thermal + Wind effects			
	DX (cm)	DY (cm)	DZ (cm)	DWD	DX (cm)	DY (cm)	DZ (cm)	DWD	DX (cm)	DY (cm)	DZ (cm)	DWD
2	3.23	-0.19	0.19	X	1.25	0.17	0.22	X	5.57	-0.53	0.24	X
3	3.29	-0.13	-0.14	X	1.18	0.08	0.15	X	5.74	-0.19	-0.35	X
4	-	-0.05	-	Yn	-	0.18	-	Y	-	-0.34	-	Yn
5	2.68	-0.3	0.63	X	1.07	0.2	0.43	X	4.68	-1.07	0.93	X
6	-	-0.07	-	Yn	-	0.13	-	Xn	-	-0.26	-	Yn
7	3.92	-0.16	0.76	X	-0.43	-0.21	0.21	X	6.74	-0.49	1.25	X
8	3.66	-0.16	1	X	1.44	0.27	0.49	X	6.23	-0.77	1.62	X
9	1.59	-0.08	1.19	X	0.59	0.1	0.50	X	2.75	-0.19	1.96	X
10	1.93	-1.35	-0.4	X	0.88	-0.38	0.14	X	3.17	-2.46	-0.82	X

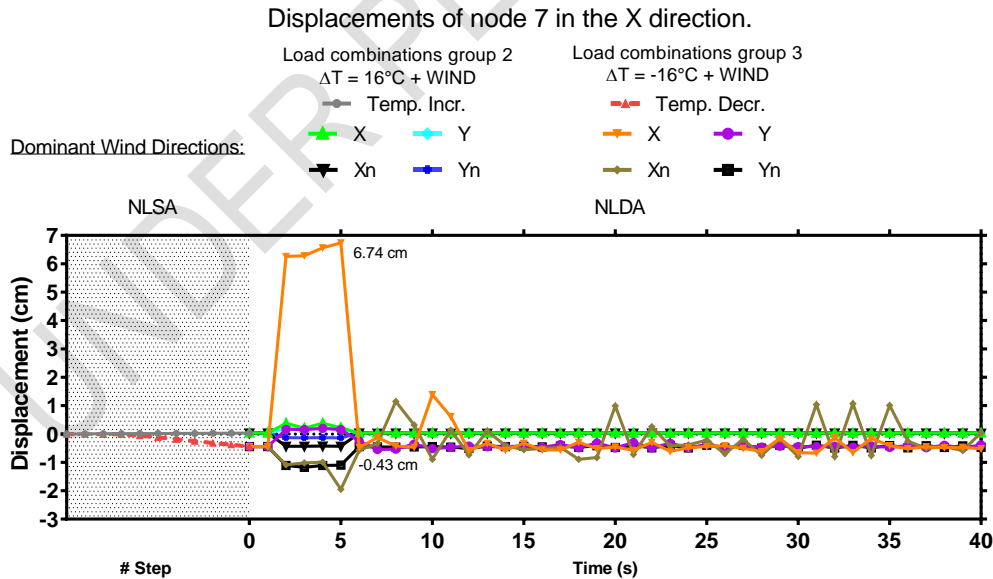
481
482
483

Since node 7 has the largest displacements in the system, the time-history records generated from this node will be analyzed for the load combinations studied. From the time-

484 history record of combo 1, it is observed that the greatest displacements occur during the
 485 excitation period in the X direction, up to 3.92 cm (Fig. 14); while, in the free vibration period,
 486 the node oscillates in a range of 0.1 cm, with a decreasing tendency around the equilibrium
 487 position. For the load combo 2.b, the displacement of the node is reduced to 0.43 cm, with
 488 oscillations around the equilibrium position of 0.1 cm. Whereas, the maximum recorded
 489 displacement occurs in the load combo 3.b, with a magnitude of 6.74 cm, where the
 490 vibrations reach a distance of 1 cm, and subsequently tend to decrease. The free nodes and
 491 the remaining support nodes, presents an analogous behavior, with minor displacements
 492 and vibrations (Fig. 15).
 493



494 **Fig. 14. Time-history record for displacements of node 7 in the X direction, load**
 495 **combination 1.**
 496
 497



498 **Fig. 15. Time-history record for displacements of node 7 in the X direction, load**
 499 **combination groups 2 and 3.**
 500
 501

502 **3.3 Spatial double layer grid behavior.**

503

504 Superstructure of the pedestrian bridge (SDLG) was modeled as a pin-jointed spatial system
 505 (see section 2.1) considering the loading conditions described in table 5, and, idealizing its
 506 behavior as a linear static system. Given these characteristics, the proposed system
 507 presents the modal behavior of table 11.

508

509 **Table 11. SDLG modal behavior**

510

Mode	Frequency (Hz)	Period (s)
1	5.49	0.182
2	8.81	0.113
3	11.21	0.089
4	13.64	0.073
5	17.30	0.058
6	20.71	0.048
11	33.49	0.030

511

512 Mode 1 presents a frequency of 5.49 Hz, and a period of 0.182 s, corresponding to the
 513 horizontal direction X. Mode 2 has a frequency of 8.81 Hz and a period of 0.113 s, relative to
 514 the vertical direction Z, while the mode 11, with a frequency of 33.49 Hz and a period of
 515 0.030 s, is associated with the horizontal direction Y. ^{AASHTO} [40] establishes that pedestrian
 516 bridges should be designed with a fundamental frequency in the vertical direction greater
 517 than 3 Hz, and in the horizontal direction, the frequency must be higher than 1.3 Hz. Thus,
 518 structural system is less likely to exhibit resonance effects and it is provided comfort to
 519 pedestrian users.

520

521 Displacements of the SDLG, for each combination of service loads, are shown in table 12.
 522 According to AASHTO (40)), vertical displacements must not exceed L/360, equivalent to
 523 6.11 cm in the analyzed bridge, while, horizontal displacements should be less that L/220,
 524 corresponding to 10 cm. The SDLG presents a maximum vertical displacement of -2.34 cm
 525 at the clear span (Fig. 16), whereas, in the horizontal direction, the maximum displacement
 526 is -0.64 cm. These values are within the permissible limits by service conditions.

527

528 **Table 12. SDLG maximum displacements**

529

Service load case	DX (cm)	DY (cm)	DZ (cm)
2	-0.24	-0.24	0.18
3	-0.61	-0.62	-2.17
5 (DT = 0°C)	-0.28	-0.28	-0.93
5 (DT = 16°C)	-0.29	-0.31	-0.77
5 (DT = -16°C)	-0.29	-0.31	-1.10
6 (DT = 0°C)	-0.61	-0.62	-2.17
6 (DT = 16°C)	-0.62	-0.64	-2.00
6 (DT = -16°C)	-0.60	-0.64	-2.34

530

531

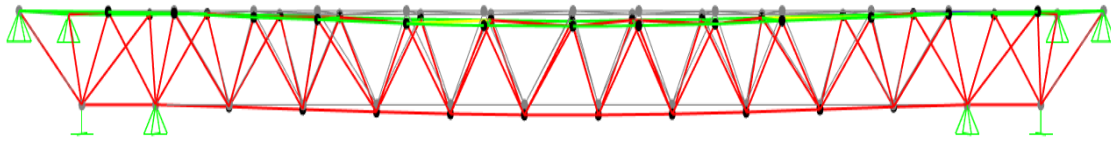


Fig. 16. SDLG vertical displacements (vertical scale 1:10).

532
533
534
535
536
537
538
539
540
541

Table 13 shows the maximum internal forces of the SDLG. Due to the boundary conditions of pin-jointed systems, axial forces are predominant in the structure. It is observed that the existence of components associated with shear forces and bending moments is caused by the application of wind forces on the structure, however, its magnitude is low.

Table 13. SDLG maximum internal forces

Type of element	Axial force (Ton)	Shear force (Ton)		Flexural moment (Ton-m)		Location	Load case
		Y	Z	Y	Z		
Top chord	26.40	0.030	0.01	0.030	0.014	Extremes	6, $\Delta T = -16^{\circ}\text{C}$
	-19.20	-0.03	-0.01	-0.030	-0.014	Span center	6, $\Delta T = +16^{\circ}\text{C}$
Diagonal	13.28	0.03	0.01	0.03	0.010	Extremes	5, $\Delta T = -16^{\circ}\text{C}$
	-15.81	-0.04	-0.01	-0.039	-0.01	Extremes	6, $\Delta T = +16^{\circ}\text{C}$
Bottom chord	33.66	0.034	0.01	0.034	0.012	Span center	6, $\Delta T = -16^{\circ}\text{C}$
	-42.95	-0.03	-0.01	-0.034	-0.012	Extremes	6, $\Delta T = +16^{\circ}\text{C}$

542
543
544
545
546
547
548
549
550
551
552
553
554
555
556
557
558
559
560
561
562
563

3.4 COUPLING OF TENSEGRITY MODULES WITH THE SDLG

In order to analyze the overall behavior of the superstructure, integrated by the SDLG and five X-T tensegrity modules, it is proposed to model the interaction of these systems, with the methodology mentioned in section 2.6, what is called in this work as system coupling. The coupling of systems consists in transmitting from one system to another, and vice versa, the mechanical effects resulting from sections 3.1 to 3.3, considering the boundary conditions defined for each structure.

On the one hand, reactions of the base nodes of the tensegrity system (see table 14), are transmitted as point forces to the receiving nodes of the SDLG, in accordance to the configuration shown in figure 2. These forces are considered as DL, applying the load combinations from table 5. The results obtained by including the effects of the TS on the SDLG, show increases in the magnitude of the displacements of the system, since, in the horizontal direction, a displacement of -0.78 cm was registered, while in the vertical direction displacement reach a value of - 2.47 cm. However, the magnitude of these displacements does not suggest a radical change in the behavior of the SDLG, since the maximum increase is 0.13 cm in the Z direction.

Table 14. Maximum reactions at the base nodes of X-T module.

Node	Fx (kg)	Fy (kg)	Fz (kg)
1	422	645	460
4	369	0	490
6	992	0	690

564

565 Table 15 shows the maximum increments of axial forces produced by the tensegrity systems
 566 in the SDLG. In the first instance, it is observed that an increase of 16°C in temperature can
 567 produce an increment up to 1180 kg (4%) in the axial force of the elements of the top chord
 568 of the SDLG. In addition, the action of the wind in the Y direction on the X-T modules,
 569 together with an increase in temperature, induces a rise of 360 kg (2%) in the diagonal
 570 members. Similarly, when integrating the wind action in the X direction with an increase or
 571 decrease in temperature, applied in the XT modules, axial force of the bottom chord
 572 elements is amplified to 950 kg (2%). Percent variations, belongs to the comparison against
 573 the results from table 13.

574
 575
 576

Table 15. SDLG maximum internal forces due coupling tensegrity systems

Type of element	Axial force (Ton)	Location	Load combination	Load case
Top chord	27.58	Extremes	CT-6	$\Delta T = 16^{\circ}\text{C}$
	-19.52	Span center	CT-6	$\Delta T = 16^{\circ}\text{C} + \text{WY}$
Diagonal	13.28	Extremes	CT-5	$\Delta T = -16^{\circ}\text{C}$
	-16.17	Extremes	CT-6	$\Delta T = 16^{\circ}\text{C} + \text{WYn}$
Bottom chord	34.39	Span center	CT-6	$\Delta T = -16^{\circ}\text{C} + \text{WX}$
	-43.90	Extremes	CT-6	$\Delta T = 16^{\circ}\text{C} + \text{WX}$

577
 578
 579
 580
 581
 582
 583
 584
 585

On the other hand, the effects that the SDLG produces in the X-T modules are displacements of the support nodes 1, 4 and 6, which are shown in table 16. The largest displacement in the X direction is 0.514 cm, in the Y direction is 0.361 cm, and, in the Z direction it is -1.898 cm. This behavior is homogeneous in the SDLG system and with a similar magnitude in all load service combinations.

Table 16. Maximum displacements on the base nodes of the X-T module.

Node	DX (cm)	DY (cm)	DZ (cm)
1	0.514	0.092	-1.898
4	0.137	0.361	-0.883
6	-0.464	-0.147	-0.504

586
 587
 588
 589
 590
 591
 592
 593
 594
 595
 596
 597
 598
 599
 600
 601
 602

By including these displacements in the support nodes of the X-T module, additional forces are induced in the system, which are distributed to each of the elements. To analyze how the behavior of the X-T module is modified, a comparison between the axial forces obtained in sections 3.1 and 3.2 against the values resulting from the coupling of the systems is presented.

When evaluating the behavior of the X-T module by only considering self-weight effects and the coupling of the systems, the force distribution shown in the Sw column of tables 17 and 18 is presented. It is noted that the compression acting on the bar-type elements (table 17), differs in a range from -4% to 0%, where the maximum decrement is 31 kg in bar 1. Regarding the type elements cable (table 18), it is seen that, in the cables 7 to 25, the difference of axial forces on average is -1%, where the maximum variation is 19 kg (-4%) on cable 9. Cable 6 has an increase of 10%, while in the cables 26 and 27, there is a decrease of -98% and -100%, respectively. This indicates that cables 26 and 27 will enter a state of inactivity (slack) during the periods in which the SDLG is deformed up to the values in table 16.

603
 604
 605
 606
 607
 608
 609
 610
 611
 612
 613
 614
 615
 616
 617

When considering the effects of wind from load combination 1, over the X-T module, in conjunction with the displacements of the support nodes caused by the coupling with the SDLG, the axial force distribution shown in column case 1 of tables 17 and 18 is presented. From this analysis, variations from -1% to 0% in the compression received by the bar elements are observed (table 17). In addition, the dominant wind direction that governs the behavior of each element is preserved. In the cable type elements (table 18), differences from -3% to 5% in axial force are presented due to the coupling of the systems; with the exception of cable 26, where the variation is -29%. Cable 7 is the only element that shows a change in the dominant wind direction.

Table 17. Maximum axial compression forces of bar elements for self-weight analysis for the load combination groups 1, 2 and 3, due coupling X-T modules with SDLG.

Sw.	Load comb. 1 ($\Delta T=0^{\circ}\text{C}$)			Load comb. group 2 ($\Delta T=+16^{\circ}\text{C}$)			Load comb. group 3 ($\Delta T=-16^{\circ}\text{C}$)		
	Wind effects			Thermal effects	Thermal + Wind effects		Thermal effects	Thermal + Wind effects	
Bar	Axial Force (kg)	Axial Force (kg)	WDD	Axial Force (kg)	Axial Force (kg)	WDD	Axial Force (kg)	Axial Force (kg)	WDD
1	1024	1367	Yn	1678	2141	Xn	497	1328	X
2	806	1030	Y	1669	1883	Y	397	1034	X
3	773	2439	X	2220	2736	X	366	2240	X
4	639	1008	Xn	1412	1780	Xn	209	866	Y
5	417	1080	X	1595	1782	Xn	365	1197	X

618
 619
 620
 621
 622
 623
 624
 625
 626
 627
 628
 629
 630
 631
 632
 633
 634
 635
 636
 637
 638
 639
 640

The differences in axial forces in the X-T module, once both systems are coupled, and by considering a 16 ° C increase in temperature, are shown in the column Case 2, thermal effects, in tables 17 and 18. For these load requirements, it can be observed that bar elements have higher order differences in the coupled case. Bar 3 is the most stressed element in the group, working under an axial force of 2220 kg, equivalent to an increase of 679 kg.

In the cable elements (table 18), increases in axial force are also exhibited. In cable 15 there is an increase of 473 kg (58%), which causes a total load of 1285 kg. In elements 18 and 19, the tension force increases 559 kg (83%) and 502 kg (91%), so these elements are subjected to a force of 1235 kg and 1054 kg. In contrast, for cables 6, 7 and 10, considerable differences are not identified, since the percentage increase in these elements ranges from -5% to 7%.

641
642
643

Table 18. Maximum axial tension forces of cable elements for self-weight analysis for the load combination groups 1, 2 and 3, due coupling X-T modules with SDLG.

Cable	Sw.	Load comb. 1 ($\Delta T=0^{\circ}\text{C}$)		Load comb. group 2 ($\Delta T=+16^{\circ}\text{C}$)			Load comb. group 3 ($\Delta T=-16^{\circ}\text{C}$)		
		Wind effects		Thermal effects	Thermal + Wind effects		Thermal effects	Wind effects	
	Axial Force (kg)	Axial Force (kg)	WDD	Axial Force (kg)	Axial Force (kg)	WDD	Axial Force (kg)	Axial Force (kg)	WDD
6	517	698	Y	837	1018	Y	209	275	X
7	486	662	Yn	775	980	Yn	165	664	X
8	445	608	Xn	448	658	Yn	126	303	Xn
9	486	659	X	845	979	X	176	672	X
10	262	597	X	422	587	X	14	386	X
11	377	654	X	813	911	Xn	73	423	X
12	369	631	X	779	868	Xn	65	399	X
13	279	620	X	420	594	X	2	374	X
14	292	560	X	861	935	Xn	192	620	X
15	410	859	X	1285	1407	Xn	299	949	X
16	124	496	X	723	865	Y	165	551	X
17	71	362	X	543	649	Xn	114	405	X
18	290	1184	X	1235	1444	X	276	1303	X
19	216	1098	X	1054	1327	X	217	1213	X
20	164	555	Xn	468	847	Xn	113	539	Xn
21	182	583	Xn	533	919	Xn	128	568	Xn
22	76	281	Xn	260	456	Xn	67	281	Xn
23	95	327	Xn	325	544	Xn	84	323	Xn
24	145	626	X	595	748	X	125	672	X
25	112	502	X	479	597	X	96	535	X
26	4	181	Y	4	181	Y	4	33	X
27	0	200	Yn	0	201	Yn	0	86	Yn

644
645
646
647
648
649
650
651
652
653
654
655
656
657

By integrating the temperature increases with the action of the wind, in the coupled system, the results of the case 2 column, Thermal + Wind effects, were obtained. Regarding the bar-elements, the bar 5 shows an increase of 672 kg (61%), working under a compression of 1782 kg. However, the most stressed element is bar 3, where an axial force of 2736 kg acts, which is 314 kg (13%) greater than that obtained before coupling the systems. Additionally, in bar 1, there is a change in the dominant wind direction of the element.

These loading conditions cause an equilibrium state where the largest increase occurring in the cable 15, since the tension increases 457 kg. Cable 18 undergo to the maximum tension forces for this load case as it works to a force of 1444 kg. Elements 6, 7, 8, 14, 15 and 17 experience changes in the dominant wind direction that causes the maximum force in these elements.

658 Moreover, by inducing a 16 ° C decrease in temperature, once the X-T module is coupled
 659 with the SDLG, the force distributions of the case 3 column, Thermal effects, are generated.
 660 The axial force of the bar elements is less than that generated by an increase in temperature
 661 (case 2). However, when compared against the forces before coupling, notable differences
 662 are perceived, since forces acting on these elements range from 365 kg to 497 kg. The
 663 increase of this magnitude implies percentage variations from 17% to 197%.
 664

665 Regarding cable type elements, two main tendencies are observed. In the cables 7 to 10,
 666 13, 26 and 27, the axial force is less than the values obtained without coupling systems. In
 667 elements 26 and 27 it is observed that they enter a period of inactivity, since the force
 668 decreases to 4 kg and 0 kg. The remaining cables have higher values compared to the point
 669 of comparison, where the largest increase is 200 kg in cable 18.
 670

671 The inclusion of the effects of the wind with temperature decreases in the coupling of the X-T
 672 module produces the state of equilibrium of forces described in the case column 3, Thermal
 673 + Wind effects of tables 17 and 18. For bar-like elements, it is observed that the differences
 674 in axial forces, originated when considering the effects of the coupling, are less than 117 kg,
 675 equivalent to -5% for bar 3. In this load condition, the dominant wind direction of bar 4 is
 676 modified.
 677

678 For cable type elements, it was identified that the difference of greatest consideration occurs
 679 in cable 26, where the axial force decreases 314 kg (-90%). Cables 18 and 19 are the only
 680 elements where occur increases in the axial force, with a magnitude of 98 kg and 94 kg. In
 681 the remaining elements, axial force variations are from an order of +/- 50 kg. In cables 6, 26
 682 and 27, modifications in the dominant wind direction were identified.
 683

684 In addition to the registered axial force variations in the components of the X-T module,
 685 differences related to the direction and magnitude of the nodal displacements are identified.
 686 Table 19 shows the displacements of each node, resulting from the coupling of the X-T
 687 module and the wind effects from load combinations 1, 2.b and 3.b.
 688

689 **Table 19. Maximum nodal displacements for the load combinations 1, 2b and 3b,**
 690 **due coupling of systems.**
 691

Node	Case 1 (dT=0°C) Wind effects				Case 2.b (dT=+16°C) Thermal + Wind effects				Case 3.b (dT=-16°C) Thermal + Wind effects			
	DX (cm)	DY (cm)	DZ (cm)	DWD	DX (cm)	DY (cm)	DZ (cm)	DWD	DX (cm)	DY (cm)	DZ (cm)	DWD
2	3.1	-0.2	0.18	X	-0.75	0.06	-0.07	Xn	4.32	-0.35	0.3	X
3	3.17	-0.13	-0.13	X	-0.76	-0.08	0.02	Xn	4.35	-0.1	-0.13	X
4	-	-0.4	-	Yn	-	-0.05	-	Yn	-	-0.1	-	Yn
5	2.56	-0.29	0.61	X	-0.77	-0.18	0.1	X	3.67	-0.38	0.9	X
6	-	-1.47	-	Xn	-	-2.12	-	Xn	-	-2.11	-	Yn
7	3.74	-0.78	0.87	X	0.45	-1.12	1.26	Xn	5.08	-1.29	1.21	X
8	3.51	-0.78	0.97	X	-0.81	-1.12	-1.17	Xn	4.8	-1.29	1.29	X
9	1.51	-0.08	1.14	X	-0.43	0.02	-0.29	Xn	2.09	-0.06	1.53	X
10	1.84	-1.3	-0.38	X	-0.54	-0.74	0.14	Xn	2.54	1.77	-0.56	X

692
 693 In the load combination 1, it is highlighted a displacement decrease in the X direction, with a
 694 value of -0.13 cm. In the Y and Z directions it is noted a slight increase in the magnitude of

695 the displacements, equal to 0.62 cm and 0.11 cm, respectively. Furthermore, a change
 696 occurs in the wind direction that produces the largest displacements.

697
 698 The nodal movements produced by the union of the systems, associated to the load
 699 combination 2.b, report displacement differences of -0.33 cm. For the free nodes, increases
 700 of up to 0.91 cm in the Y direction, and, 1.05 cm for the Z direction, are distinguished. In this
 701 group of nodes (with the exception of node 6), changes in the dominant wind direction occur.
 702

703 From the results corresponding to the coupling of systems with the loading conditions of
 704 case 3.b, it is observed that, due to the distribution of forces that occur in the system under
 705 these conditions, leads to the reduction of displacements of - 1.15 cm on average. In node 7
 706 the displacements are reduced to -1.66 cm. Unlike the previous cases, the dominant wind
 707 directions that produce maximum displacements are not altered.
 708

709 In particular, the displacements of the support nodes 1, 4 and 6 were evaluated, since they
 710 exhibit a different behavior from that of the free nodes. Both node 4 and node 6, have
 711 freedom of movement in the Y direction, therefore, in load combination 1, there are
 712 increases of 0.35 cm and 1.40 cm, respectively. For the load combination 2.b, the magnitude
 713 of the displacement of node 4 is decreased by -0.13 cm. However, node 6, the maximum
 714 variation of 1.99 cm is presented, which implies a displacement of 2.12 cm. Similarly, at the
 715 combination 3.b, in node 4 there is a decrease of -0.24 cm, and node 6 shows an increase of
 716 1.85 cm.
 717

718 **4. DISCUSSIONS**

719
 720 From this work, it is highlighted as a discussion that the results obtained show congruence
 721 and extend what was reported by the research of Ashwear and Eriksson [13], and with those
 722 of Lazzari *et al.* [5].
 723

724 The research of Ashwear and Eriksson [13], is oriented in to the study of 2D tensegrity
 725 systems under temperature variations, associated with temperature decreases of 45°C and
 726 increments of 26°C. It is reported that, according to the boundary conditions of the support
 727 nodes, and, the relationship between the coefficient of thermal expansion of the bars with
 728 that of the cables, the behavior of the assembly can be described by one of the categories
 729 shown in table 20.
 730

731 **Table 20. Structural behavior of 2D tensegrity systems under environment**
 732 **temperature variations (adapted from Ashwear and Eriksson [13][13]).**
 733

Thermal Expansion coefficient relations	Boundary conditions of bar and cable elements' nodes		
	Fixed - Free	Fixed - Fixed	Fixed – Fixed (Supports)
ab = ac	No variation		
ab < ac	Temp. increase → Axial force reduces		Temp. increase → Axial force rises
	Temp. decrease → Axial force rises		
ab > ac	Temp. increase → Axial force rises		Temp. decrease → Axial force reduces
	Temp. decrease → Axial force reduces		

734
 735 Considering the boundary conditions of the X-T module, which has one articulated support
 736 (fixed to movement) node and two other supports with freedom of movement only in the Y
 737 direction; in addition, to a relationship of thermal expansion coefficients expressed as $\alpha_b >$

738 α_c , it can be observed that behavior of the X-T module matches with one the categories
739 from table 20. However, it is noted that when performing analysis of a 3D tensegrity system,
740 additional features are identified to those reported by Ashweat and Eriksson [13].

741

742 Although, the overall behavior of the structural system is acts accordance with previously
743 described work , it is observed that, at an increase in temperature, the axial force of some
744 elements may decrease, while, under a decrease in temperature, the axial force of certain
745 elements increases. This phenomenon occurs, due to the fact that the spatial position of the
746 X-T module, under the thermal variations studied, implies that the nodes that define
747 elements 26 and 27 approach or move away, which causes increases or decreases in axial
748 force.

749

750 In the research of Lazzari *et al.* [5] quasi-static analyzes of the effects of wind on the roof of
751 the La Plata stadium were performed. The wind was considered as random points for a time
752 of 40 s, representing the stochastic nature of the wind, with a logarithmic behavior. From
753 their results, it is emphasized that by using this methodology it was feasible to identify the
754 maximum nodal displacements and the highest stresses for bars and cables. In addition, it
755 was identified that on some cable elements the tensile forces are reduced to a null value,
756 when wind acts in a specific direction.

757

758 This behavior is consistent with the results obtained in this investigation, since, due to the
759 conditions and the asymmetry of the assembly, each element is governed by a specific wind
760 direction. The advantage of using dynamic models is that they allow to evaluate the behavior
761 of the system when is loaded and in the free vibration period, which is used to determine, in
762 a simple way, the stability of the assembly.

763

764 The most drastic effects implied by the coupling of the five X-T modules with the SDLG, are
765 the increases in node displacements and in the axial forces of the structural elements. It was
766 recorded a movement of 2.12 cm for node 6, which must be considered when designing the
767 base node connection devices. Additionally, compression force in bar 3 rises up to 2736,
768 while, tension in cable 18 reaches a value of 1444 kg. These axial forces determine the
769 cross-section of each type of elements.

770

771 It is important to highlight the following discussions about the proposed methodology for the
772 coupling of the systems. SDLG is a system that presents a linear behavior within the elastic
773 range. Therefore, it is feasible to use the principle of superposition, to transmit the loads
774 generated by the tensegrity systems. This allowed to calculate the displacements and the
775 forces developed in the SDLG.

776

777 However, for the X-T module, although its components remain within the elastic range, the
778 system is intrinsically non-linear and manifests large displacements, so that the principle of
779 effect superposition is not suitable for modeling the coupling. Therefore, the proposed
780 method to determine with greater approximation, the axial forces and the nodal movements,
781 which occur in the X-T module, due to the coupling, was through non-linear dynamic models,
782 representing the maximum displacements of the SDLG, as a base movement dynamic
783 problem. The limitation of implementing these methods is that the modal behavior of the
784 complete assembly is unknown.

785

786 **5. CONCLUSION**

787

788 By means of non-linear static analyses, it was feasible to define the boundary conditions for
789 the base node of the X-T module, which allows to couple the TS with the SDLG. Restricting
790 the degrees of freedom in the vertical direction (Z direction) and in the transverse direction

791 (X direction) reduces the displacements of the support nodes of the X-T module, thereby
792 preserving the internal area designated for the pedestrian crossing. In addition, it allows the
793 system to distribute the internal forces evenly and the assembly to continue working
794 according to the mechanical principles of the tensegrity structures, that is, that the bar-like
795 elements work only under compression and the cables under tensile forces.

796
797 Through static analyzes of the SDLG, and non-linear dynamic analyses of TS, the internal
798 forces and the structural response were obtained, generated by the integration of wind
799 effects and variations of temperature in each system.

800
801 The methodology used to develop the coupling of the tensegrity modules with the
802 superstructure of the pedestrian bridge, allowed to determine the effects caused by the
803 interaction of both systems. As well as maximum displacements and internal forces in each
804 system. Through this methodology, the characteristics necessary to generate the connection
805 devices were defined, according to the idealizations made in the finite element models.
806 Through this methodology the necessary conditions to generate the connection devices
807 were defined, according to the idealizations made in the finite element models.

808
809 From the non-linear dynamic analysis performed for the X-T module, it is denoted the
810 capacity of this system to return to its initial equilibrium state, once the excitation period is
811 over. The ability of the X-T module to return to the initial equilibrium state is highlighted, once
812 the excitation period is over. This fact allows to define that the generated tensegrity system
813 shows a stable behavior under the proposed working conditions.

814
815 When determining the maximum axial force in each member of the module, the geometric
816 cross sections were defined, which ensure a behavior in the elastic range of each element,
817 and thus avoid exceeding the critical load that would cause instability in the system, as
818 effects buckling in the bar elements; while, yielding and rupture are avoided in cables.

819
820
821

822 **COMPETING INTERESTS**

823 Authors declare that no competing interests exist.

824
825
826

827 **REFERENCES**

828

- 829 1. Jáuregui Gómez V. Tensegrity Structures and their Application to Architecture.
830 2004;1–239. Available from: [http://www.tensegridad.es/Publications/MSc_Thesis-](http://www.tensegridad.es/Publications/MSc_Thesis-Tensegrity_Structures_and_their_Application_to_Architecture_by_GOMEZ-JAUREGUI.pdf)
831 [Tensegrity_Structures_and_their_Application_to_Architecture_by_GOMEZ-](http://www.tensegridad.es/Publications/MSc_Thesis-Tensegrity_Structures_and_their_Application_to_Architecture_by_GOMEZ-JAUREGUI.pdf)
832 [JAUREGUI.pdf](http://www.tensegridad.es/Publications/MSc_Thesis-Tensegrity_Structures_and_their_Application_to_Architecture_by_GOMEZ-JAUREGUI.pdf)
- 833 2. Bel Hadj Ali N, Rhode-Barbarigos L, Pascual Albi AA, Smith IFC. Design optimization
834 and dynamic analysis of a tensegrity-based footbridge. Eng Struct [Internet].
835 2010;32(11):3650–9. Available from:
836 <http://dx.doi.org/10.1016/j.engstruct.2010.08.009>
- 837 3. De Boeck J. Tensegrity bridges. Delft. University of Technology; 2013.
- 838 4. Motro R, Raducanu V, Fuller RB. Tensegrity Systems. 2003;18(2):77–84.
- 839 5. Lazzari M, Vitaliani R V., Majowiecki M, Saetta A V. Dynamic behavior of a tensegrity
840 system subjected to follower wind loading. Comput Struct. 2003;81(22–23):2199–
841 217.
- 842 6. Australian Steel Institute. Kurilpa Bridge , Brisbane Structural Engineering Award
843 2010 (Qld). 2010;2010.

- 844 7. Korkmaz S, Ali NBH, Smith IFC. Self-repair of a tensegrity pedestrian bridge through
845 grouped actuation. Proc Int Conf Comput Civ Build Eng Nottingham, UK.
846 2010;(1987):449.
- 847 8. Chen L-H, Kim K, Tang E, Li K, House R, Zhu EL, et al. Soft Spherical Tensegrity
848 Robot Design Using Rod-Centered Actuation and Control. J Mech Robot. 2017;9(2).
- 849 9. Tran HC, Lee J. Geometric and material nonlinear analysis of tensegrity structures.
850 Acta Mech Sin Xuebao. 2011;27(6):938–49.
- 851 10. Murakami H. Static and dynamic analyses of tensegrity structures. Part 1. Nonlinear
852 equations of motion. Int J Solids Struct. 2001;38(20):3599–613.
- 853 11. Murakami H. Static and dynamic analyses of tensegrity structures. Part II. Quasi-
854 static analysis. Int J Solids Struct. 2001;38(20):3615–29.
- 855 12. Lu CJ, Wang XD, Lu SN. Wind-Induced Dynamic Analysis of the Flat Tensegrity
856 Structures in Time Domain. Appl Mech Mater [Internet]. 2012;166–169:140–3.
857 Available from: <http://www.scientific.net/AMM.166-169.140>
- 858 13. Ashwear N, Eriksson A. Influence of temperature on the vibration properties of
859 tensegrity structures. Int J Mech Sci [Internet]. 2015;99:237–50. Available from:
860 <http://dx.doi.org/10.1016/j.ijmecsci.2015.05.019>
- 861 14. Zhang Z, Dong S, Fu X. Structural Design of a Spherical Cable Dome With Stiff Roof.
862 Int J Sp Struct. 2007;22(3):45–56.
- 863 15. Rhode-Barbarigos L, Hadj Ali NB, Motro R, Smith IFC. Tensegrity modules for
864 pedestrian bridges. Eng Struct. 2010;32(4):1158–67.
- 865 16. Tibert AG, Pellegrino S. Review of Form-Finding Methods for Tensegrity Structures.
866 Int J Sp Struct [Internet]. 2011;26(3):241–55. Available from:
867 <http://journals.sagepub.com/doi/10.1260/0266-3511.26.3.241>
- 868 17. Gomez Estrada G. Analytical and numerical investigations of form-finding methods
869 for tensegrity structures. 2007;152.
- 870 18. Yuan X, Chen L, Dong S. Prestress design of cable domes with new forms. Int J
871 Solids Struct. 2007;44(9):2773–82.
- 872 19. Ochoa Peralta LA, Orellana Ochoa PF. Tensegriedad como sistema estructural
873 alternativo aplicado a cubiertas. Universidad de Cuenca; 2017.
- 874 20. Cobos JI. Tensegriedad como sistema estructural alternativo aplicado a puentes
875 peatonales. UNIVERSIDAD DE CUENCA; 2018.
- 876 21. Connelly R. Globally Rigid Symmetric Tensegrities Tensegrites symetriques
877 globalement rigides. Struct Topol. 1995;21:59–78.
- 878 22. Connelly R, Whiteley W. Second-Order Rigidity and Prestress Stability for Tensegrity
879 Frameworks. SIAM J Discret Math [Internet]. 1996;9(3):453–91. Available from:
880 <http://epubs.siam.org/doi/10.1137/S0895480192229236>
- 881 23. Deng H, Kwan ASK. Unified classification of stability of pin-jointed bar assemblies. Int
882 J Solids Struct. 2005;42(15):4393–413.
- 883 24. Zhang JY, Ohsaki M. Stability conditions for tensegrity structures. Int J Solids Struct.
884 2007;44(11–12):3875–86.
- 885 25. Lazopoulos KA. Stability of an elastic tensegrity structure. Acta Mech. 2005;179(1–
886 2):1–10.
- 887 26. Amendola A, Carpentieri G, de Oliveira M, Skelton RE, Fraternali F. Experimental
888 investigation of the softening-stiffening response of tensegrity prisms under
889 compressive loading. Compos Struct. 2014;
- 890 27. Zhang L, Zhang C, Feng X, Gao H. Snapping instability in prismatic tensegrities
891 under torsion. Appl Math Mech (English Ed. 2016;37(3):275–88.
- 892 28. Atig M, El Ouni MH, Ben Kahla N. Dynamic stability analysis of tensegrity systems.
893 Eur J Environ Civ Eng [Internet]. 2017;8189(March):1–18. Available from:
894 <http://dx.doi.org/10.1080/19648189.2017.1304275>
- 895 29. Secretaria de Comunicaciones y Transportes. N-PRY-CAR-6-01-003/01 Cargas y
896 Acciones. In: Proyectos de Nuevos Puentes y Estructuras Similares. 2001. p. 1–25.

- 897 30. Pellegrino S, Calladine CR. Matrix analysis of statically and kinematically
898 indeterminate frameworks. *Int J Solids Struct.* 1985;22:409–28.
- 899 31. Calladine CR, Pellegrino S. First-order infinitesimal mechanisms. *Int J Solids Struct*
900 [Internet]. 1991;27(4):505–15. Available from:
901 <http://linkinghub.elsevier.com/retrieve/pii/0020768391901375>
- 902 32. Kebiche K, Kazi-Aoual MN, Motro R. Geometrical non-linear analysis of tensegrity
903 systems. *Eng Struct.* 1999;21(9):864–76.
- 904 33. Cook RD, Malkus DS, Plesha ME, Witt RJ. *Concepts and Applications of Finite
905 Element Analysis.pdf.* John Wiley & Sons I, editor. 2002. 733 p.
- 906 34. Cook RD, Saunders H. *Concepts and Applications of Finite Element Analysis.* Sons
907 JW&, editor. Vol. 106, *Journal of Pressure Vessel Technology.* 2009. 127 p.
- 908 35. Craig RRJ, Kurdila AJ. *Fundamentals of Structural Dynamics. Flow Induced Vibration
909 of Power and Process Plant Components.* John Wiley & Sons; 2011. 37–62 p.
- 910 36. Clough RW, Penzien J. *Dynamics of structures.* Computers & Structures, Inc.; 1995.
- 911 37. SAP2000. *Computers & Structures, Inc.* [Internet]. Available from:
912 <https://www.csiespana.com/software/2/sap2000>
- 913 38. Secretaria de Comunicaciones y Transportes. N-PRY-CAR-6-01-004/01 Viento. In:
914 *Proyectos de Nuevos Puentes y Estructuras Similares.* 2001. p. 1–18.
- 915 39. INEGI [Internet]. Available from:
916 <http://cuentame.inegi.org.mx/monografias/informacion/queret/territorio/clima.aspx?tema=me&e=22>
- 917
918 40. AASHTO. *Guide Specifications for Design of Pedestrian Bridges.* 2009 p. 40.
919
920